ELSEVIER

Polymer 42 (2001) 9633–9640

polymer

www.elsevier.com/locate/polymer

A hierarchical structure and properties of intercalated polypropylene/clay nanocomposites

Pham Hoai Nam[a], Pralay Maiti[a], Masami Okamoto[a,*], Tadao Kotaka[a], Naoki Hasegawa[b], Arimitsu Usuki[b]

[a]*Advanced Polymeric Materials Engineering, Graduate School of Engineering, Toyota Technological Institute, Hisakata 2-12-1, Tempaku, Nagoya 468-8511, Japan*

[b]*Toyota Central R & D Laboratories, Inc., Nagakute, Aichi 480-1192, Japan*

Received 9 April 2001; accepted 10 May 2001

Abstract

We have prepared the intercalated nanocomposites of polypropylene (PP)/clay (PPCNs) successfully using maleic anhydride modified PP (PP-MA) and organophilic clay via melt extrusion process. The hierarchical structure of the PPCNs from the structure of confined PP-MA chains, in the space a few nanometer width between silicate galleries to crystalline lamellae of 7–15 nm thickness and spherulitic texture of 10 μm diameter, were probed using a wide-angle X-ray diffraction, small-angle X-ray scattering, transmission electron microscope, polarizing optical microscopy and light scattering. After crystallization had taken place at 80°C, the PPCNs formed rod-like crystalline texture in the 10 μm length scale which consisted of the inter-fibrillar structure including γ-phase crystallite caused by the reduction of the PP-MA chains mobility due to the intercalation of the PP chains in the space between silicate galleries and the narrow space surrounded by the dispersed clay particles. The intercalated PPCNs showed an enhancement of moduli compared with PP matrix without clay. The necessity of the intercalating degree of PP-MA chains on the enhancement of the mechanical properties are discussed.

Keywords: Polypropylene; Nanocomposite; Intercalation

1. Introduction

Development of the polymer/clay nanocomposites is one of the latest evolutionary steps of the polymer technology. The nanocomposites offer attractive potential for diversification and application of conventional polymeric materials [1–5]. Since the possibility of direct melt intercalation was first demonstrated by Giannelis et al. [6], the melt intercalation method has become a main stream for the preparation of the intercalated polymer nanocomposites without in situ intercalative polymerization. It is a quite effective technology for the case of polyolefin-based nanocomposites [7,8].

In recent years, intensive studies have been devoted to the complete exfoliation of the stacked silicate layers in the polymer matrix under the advanced preparation method [9,10]. We have successfully prepared well-ordered intercalated polypropylene (PP)/clay nanocomposites (PPCN)s [7] via direct melt intercalation in an extrusion process, where the layered clay particles were dispersed homogeneously in the PP matrix and intercalated by extended PP chains. The PP-based intercalated nanocomposites have attractive potentials for continuous expansion of application versatility [11]. Although the dispersed morphology of the clay particles, the excellent mechanical properties [7,8] and the rheological behavior [12,13] of the intercalated PPCNs were investigated, the hierarchical structure for PPCNs viewed on scale from nm to μm length, i.e. from the structure of confined PP chains in the space of the silicate galleries of a few nm width to crystalline lamellae of about 10 nm thickness and spherulitic texture of several μm diameter, has not been identified in detail. For innovation of PPCNs, we have to understand the structural details and create a technology of controlling the hierarchical structure of the PPCNs.

In this study, we prepared the intercalated PPCNs using maleic anhydride modified PP and organophilic clay via melt extrusion processing and conducted identification of the hierarchical structure in detail. We also discuss here the structure–property relationships of the intercalated PPCNs having different clay content.

* Corresponding author. Tel.: +81-52-809-1861; fax: +81-52-809-1864.
E-mail address: okamoto@toyota-ti.ac.jp (M. Okamoto).

0032-3861/01/$ - see front matter
PII: S0032-3861(01)00512-2

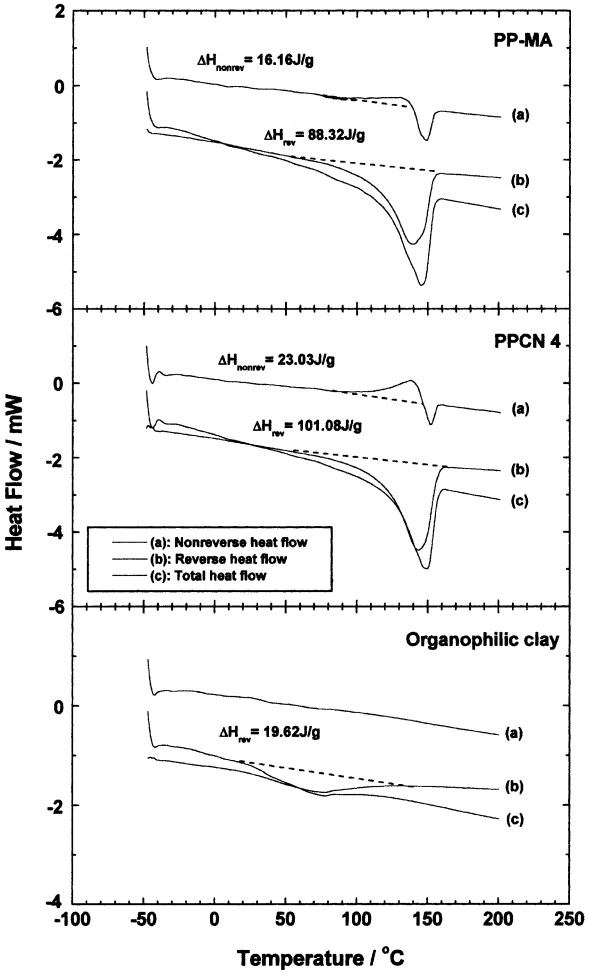

Fig. 1. TMDSC scan for organophilic clay, PP-MA, and PPCN4: (a) nonreversing heat flow; (b) reversing heat flow; and (c) total heat flow.

2. Experimental

2.1. Materials and preparation

The organophilic clay used in this study, which was synthesized by an ion exchange reaction between Na^+-montmorillonite with a cation exchange capacity of 110 meq/100 g and stearyl ammonium chloride, was supplied by Nanocor Inc. The PP modified by 0.2% maleic anhydride (MA) (PP-MA) was a commercial product from Exxon Chemical. The weight average molecular weight M_w ($=19.5\times10^4$) and polydispersity index $M_w/M_n(=2.98)$ were determined by high temperature gel permeation chromatography (GPC: Tosoh HLC-8121 GPC/HT) using *o*-dichlorobenzene carrier at 145°C with polystyrene (PS) elution standards. The PPCNs with three different clay content (inorganic parts) of 2, 4 and 7.5 wt%, which were correspondingly abbreviated as PPCN2, PPCN4 and PPCN7.5, respectively, were extruded at 200°C using a twin-screw extruder (TEX30α-45.5BW, Japan Steel Works Ltd). The extruded and pelletized strands were dried under vacuum at 70°C to remove water. The pellets were pressed into sheets under pressure of ~1 MPa in hot press for 3 min at 180°C (above melting temperature of PP-MA). Then molded sheet of ~2 mm thick was quickly quenched in ice-water and annealed at 80°C for 1 h to crystallize isothermally before being subjected to all measurements.

2.2. Characterization methods

The melting temperature, T_m and the degrees of crystallinity, χ_c of the intercalated PPCNs were determined by a temperature-modulated differential scanning calorimeter (TMDSC) (MDSC™, TA2920, TA Instruments) operating at a heating rate of 5°C/min with a heating/cooling cycle of modulation period 60 s and an amplitude of ±0.796°C. To estimate χ_c in the test specimens, before performing the DSC analysis, we have to subtract the extra heat absorbed by the crystallites formed during heating process from the total endothermic heat flow due to the melting of the whole crystallites. This can be done using TMDSC. The principles and procedures are found in the relevant literatures, for example, by Wunderlich [14]. A brief description of TMDSC applied to semicrystalline *syndiotactic* polystyrene was reported in our previous publication [15]. In the TMDSC experiments, shown in Fig. 1, the endothermic heat flow ΔH_{diff} of the initially existing crystallites can be easily calculated as $\Delta H_{diff} = \Delta H_{rev} - \Delta H_{nonrev}$, where ΔH_{rev} is the endothermic melting (reversing) enthalpy from the reversing heat flow profile and ΔH_{nonrev} is the exothermic ordering/crystallization (nonreversing) enthalpy from the nonreversing heat flow profile appearing in the temperature range 70–150°C. One illustrating calculation that can be shown here is the case of the PP-MA. The observed enthalpies were $\Delta H_{rev} = 88.32\ J/g$ and $\Delta H_{nonrev} = 16.16\ J/g$. The χ_c was thus calculated as $\Delta H_{diff}/\Delta H^0 = 43.73\%$ with $\Delta H^0 = 165\ J/g$, which is the melting enthalpy of 100% crystalline PP [11]. In the case of intercalated PPCNs, the reversing and nonreversing enthalpies obtained from TMDSC experiments were recalculated for the crystallization originating from only matrix polymer. The estimated values of χ_c in the case of nanocomposites thus estimated are shown later in Table 1. In the TMDSC scan for the organophilic clay, a broad peak appeared at the temperature range 50–90°C. This peak is attributed to the melting of stearyl ammonium intercalated in the silicate layers.

Wide-angle X-ray diffraction (WAXD) experiments were performed for the organophilic clay and intercalated PPCNs using a MXlabo diffractometer (MAC Science Co.), which has an X-ray generator of 3 kW, a graphite monochromator, CuKα radiation (wavelength, $\lambda = 0.154$ nm) and operating at 40 kV and 20 mA. The samples were scanned at a scanning speed of 2°/min under the diffraction angle 2Θ in the range of 1–70°.

Small-angle X-ray scattering (SAXS) experiments were

Table 1
Characteristic parameters of organophilic clay, PP-MA, and PPCNs

Property	Organophilic clay	PP-MA	PPCN2	PPCN4	PPCN7.5
Clay content (vol%)		0	0.75	1.54	2.95
T_m (°C)	30–100[a]	138.6	139.5	143.2	143.9
χ_c (%)		43.7	40.4	47.2	48.7
TEM					
d_{clay}[b] (nm)			5.2 ± 0.4	7.9 ± 0.6	10.2 ± 1.8
L_{clay}[c] (nm)			193.3 ± 25.0	158.9 ± 24.8	127.3 ± 21.4
(L_{clay}/d_{clay})			37.2	20.1	12.5
ξ_{clay}[d] (nm)			61.7 ± 20.0	49.5 ± 10.8	34.6 ± 12.4
SAXS					
$d_{lamellae}$ (nm)		7.12	7.21	7.24	7.36
$L_{lamellae}$ (nm)		15.0	14.8	15.0	15.0
$\phi_c(\equiv d_{lamellae}/L_{lamellae})$ (%)		47.5	48.7	48.3	49.0
Q_{SAXS}		4.90	4.50	4.85	5.35
WAXD					
$d_{(001)}$ (nm)	2.31		3.24	3.03	2.89
χ_γ[e] (%)		0	0	6.7	10.5

[a] Melt temperature range of stearyl ammonium intercalated in silicate galleries.
[b] Average thickness of the dispersed clay particles.
[c] Average length of the dispersed clay particles.
[d] Correlation length of the dispersed clay particles.
[e] Relative percentage content of the γ-phase crystallite.

also conducted to characterize the crystalline morphology for the nanocomposites. The SAXS profiles were obtained by a M06XCE instrument consisting of a 6 kW rotating-anode X-ray generator (MAC Science Co.) with CuKα radiation (wavelength, $\lambda = 0.154$ nm) and operating at 50 kV and 24 mA. This apparatus includes a Ge monochromator, a point focusing optics, and a vacuum chamber for the incident beam path and scattered beam path and a two-dimensional imaging plate detector. The distance between the sample and the detector was set as 550 mm. The correction for slit-width smearing was not needed due to the fine cross-section (0.1mm × 1mm) of the primary X-ray beam used in this study, but the obtained data were corrected for sample absorption. The exposure time for measuring each sample was 1 h.

To clarify the nanoscale structure of the intercalated PPCNs, a transmission electron microscope (TEM) (H-7100, Hitachi Co.) was also used, and operated at an accelerating voltage of 100 kV. The ultrathin sections with a thickness of 100 nm were microtomed at −80°C using a Reichert Ultracut cryoultramicrotome with staining.[1]

To investigate the spherulitic texture, the PP-MA and nanocomposites were subjected to light scattering (LS) measurement under Hv scattering mode and polarizing optical microscopy (POM) observation. The details of LS measurement systems were described in our previous paper [16].

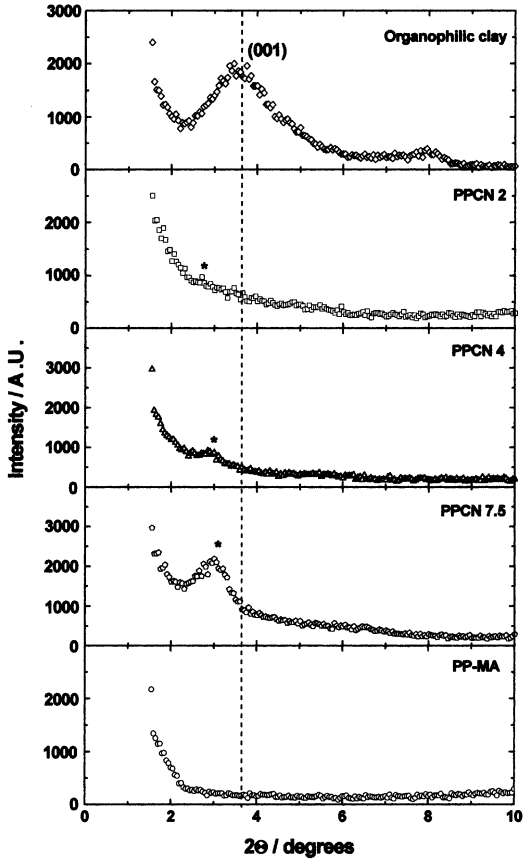

Fig. 2. WAXD patterns for organophilic clay, PP-MA, and PPCNs. The dashed lines indicate the location of the silicate (001) reflection of organophilic clay. The asterisks indicate a remnant shoulder for PPCN2 or a small peak for PPCN4.

[1] Due to high gas barrier property of the PPCNs, the staining with an RuO_4 vapor at 5°C for long time (~48 h) was not sufficient to distinguish the crystalline lamellae.

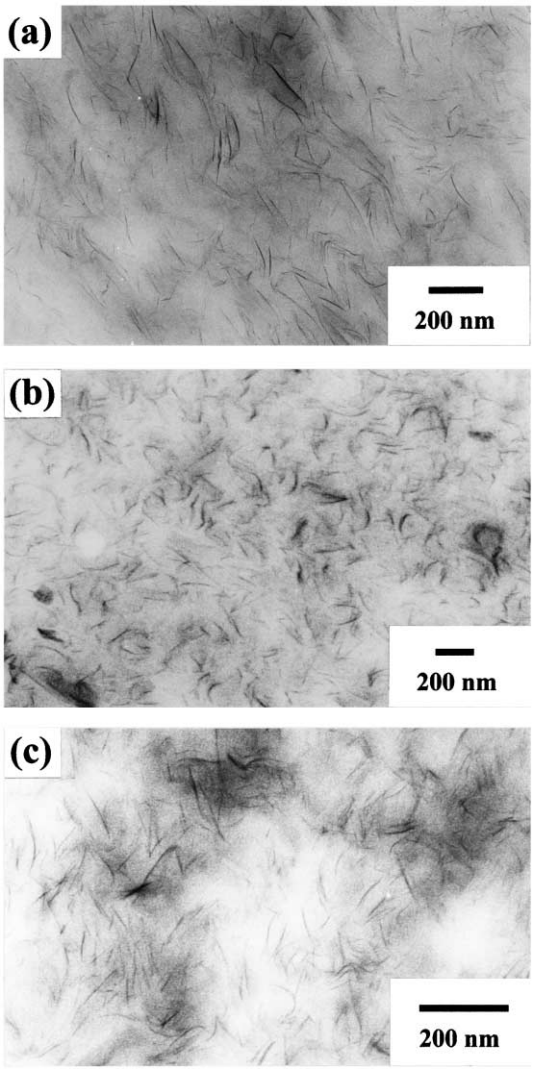

Fig. 3. TEM micrographs showing PPCNs for: (a) PPCN2, (b) PPCN4, and (c) PPCN7.5. The dark lines are the cross-sections of silicate layers and the bright areas are the PP-MA matrix.

Dynamic mechanical properties of the intercalated PPNCs were measured by using a Reometrics Dynamic Analyzer (RDAII) in the tension–torsion mode. The experiments of the temperature dependence of dynamic storage (G'), loss (G'') and their ratio, tan δ were conducted at a constant frequency ω of 6.28 rad/s with strain amplitude of 0.05% and in the temperature range -50 to 160°C, with a heating rate of 2°C/min.

3. Results and discussion

3.1. WAXD patterns and TEM observation

Fig. 2 shows the results of XRD patterns in the range of $2\Theta = 1$–10°. The mean interlayer spacing of the (001) plane ($d_{(001)}$) for the organophilic clay solid obtained by WAXD measurements is 2.31 nm ($2\Theta = 3.82°$). The pattern of PP-MA is displayed as a baseline to compare the existence of diffraction peaks coming from the dispersed clay in the polymeric matrix. For PPCN2 and PPCN4, a small remnant shoulder is observed around $2\Theta \cong 2.7°$ and a small peak at $2\Theta \cong 2.9°$, respectively, corresponding to the (001) plane of silicate layers in the PP-MA matrix. In the PPCN7.5, the strong diffraction peak is observed as a well-defined peak at $2\Theta \cong 3.05°$ ($\cong 2.89$ nm), implying that the ordered intercalated nanocomposite was formed. For the case of PPCN2 and PPCN4, we can also conclude that the PP-MA polymer chains were intercalated in the silicate galleries and the coherent order of the silicate layers is much lower compared to that of PPCN7.5. These features are clearer in the results of TEM bright field images corresponding to the WAXD experiments as shown in Fig. 3. For each PPCN, we observed fine and uniform dispersion of the clay particles in the polymer matrix where most of the clay particles (edges of the silicate layer) exhibit perpendicular alignment to the sample surface. Obviously, for PPNC4 and PPNC7.5, the stacked silicate layers are observed. We summarized the form factors obtained from TEM pictures, i.e. length L_{clay} and thickness d_{clay} of the dispersed clay particles and the correlation length ξ_{lay} between the dispersed layers in Table 1. With increasing clay content, L_{clay} decreases in the range 193–127 nm accompanied with stacking of individual silicate layers, which have an original thickness of ~1 nm and an average length of ~150 nm. ξ_{lay} value of the PPCN7.5 becomes half compared to that of PPCN2, suggesting the spatial-linked like structure of the dispersed clay particles is formed. Dividing the value of d_{clay} by $d_{(001)}$ value of each PPCN, we can estimate the number of the

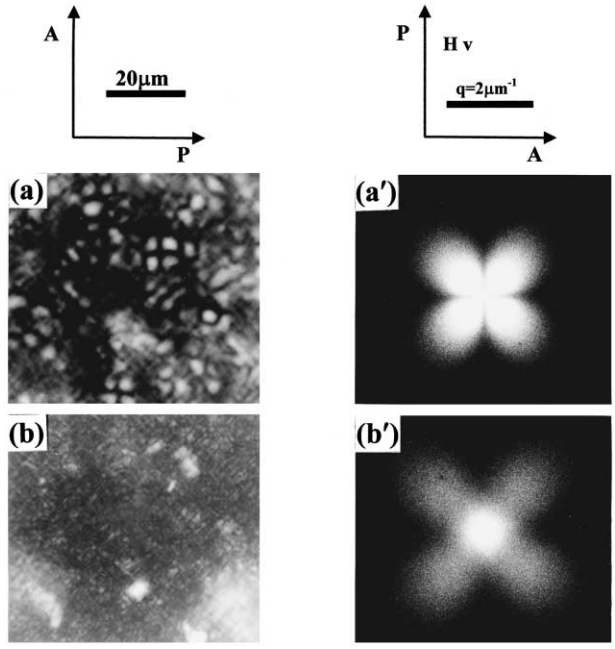

Fig. 4. Polarized optical micrographs ((a) and (b)) and the corresponding Hv–LS patterns ((a′) and (b′)) for PP-MA and PPCN4 isothermally crystallized at 80°C for 1 h, respectively.

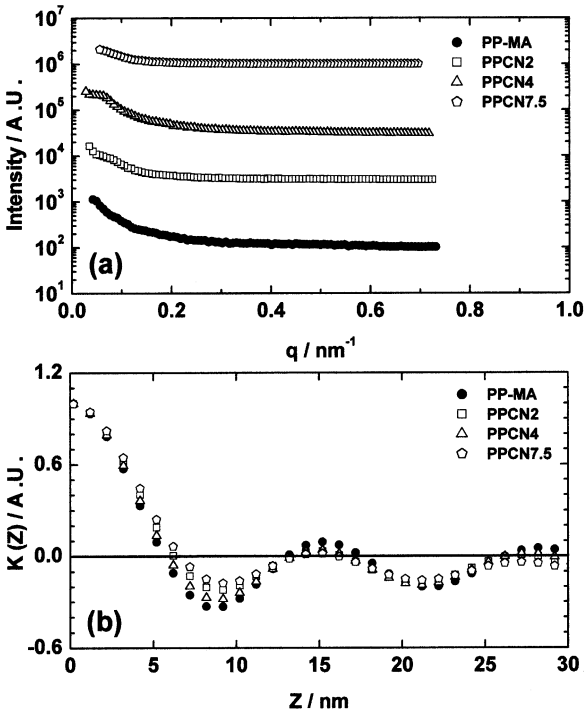

Fig. 5. SAXS data for PP-MA and PPCNs: (a) scattering profile where the data in the *y*-axis direction was shifted by a factor of 10 to avoid the overlap; and (b) normalized one-dimensional electron density correlation function $K(z)$ obtained from Eq. (1).

stacked individual silicate layers of about two for PPCN2 and about four for the case of PPCN7.5. The coherent order of the stacked layers strongly depends on the clay content. From WAXD and TEM analyses, the extent of exfoliation and/or stacking of the clay particles in this system are controlled by the amount of clay. The grafted polar-groups (maleic anhydride) in the PP-MA chains promoted the interaction with clay particles by diffusion of PP chain into the space between silicate galleries (intercalating sites) [7,8], therefore, the decrement of intercalating sites leads to the exfoliation toward the individual silicate layers.

3.2. Crystallite morphology

Fig. 4 shows the typical example of the POM micrographs [(a) and (b)] and the corresponding LS patterns [(a′) and (b′)] under Hv optical alignment for PP-MA and PPCN4, respectively, isothermally crystallized at 80°C for 1 h, for which the crystallization had been completed. The clear spherulites with positive birefringence appeared in POM and the four-leaf-clover patterns of Hv–LS were seen for the crystallized PP-MA. It is well known that at low crystallization temperature (~85°C), neat PP crystallizes to form positive spherulites which consist of crosshatch lamellae branching, i.e. subsidiary lamellae grows tangentially to the radiating primary lamellae [17]. The clear four-leaf-clover pattern is due to the high ordering of both tangential and radial lamellae in the spherulite [17].

In contrast, for PPCN4, the diffuse maltese cross patterns with very weak positive birefringence is seen in Fig. 4b and the rod-like pattern is observed clearly in Fig. 4b′ rather than four-leaf-clover pattern. The rod-like scattering pattern is ascribed to the parallel arrangement of radiation primary lamellae and the disordered arrangement of crosshatch lamellae, while the weak positive birefringence is attributed to the low density of the crosshatched lamellae. The formation of the crosshatch lamellae may be restricted due to small space surrounded by the dispersed clay particles ($\cong\xi_{clay}$) in the PPCN matrix. These interesting features may be related to the formation of γ-phase crystallite [11] of the crystallized PPCNs. This will be discussed later.

Other interesting features are the crystallization kinetics of the intercalated PPCNs and a potential of the dispersed clay particles for nucleating agents under isothermal crystallization condition. Such discussion is beyond the objective of this paper, and we will report it separately [18].

Fig. 5a shows the one-dimensional SAXS patterns obtained from the crystallized PPCNs, and Fig. 5b is the corresponding normalized one-dimensional correlation function calculated by the method of Strobl [19]. The normalized correlation function $K(z)$ is given by Ref. [20] as

$$K(z) = \frac{\int_0^\infty s^2 j(s)\cos(2\pi z s)\,\mathrm{d}s}{\int_0^\infty s^2 j(s)\,\mathrm{d}s} \tag{1}$$

where s, λ, 2θ, and $j(s)$ are the reciprocal-space coordinate ($s = 2\sin\theta/\lambda$), the X-ray wavelength, the scattering angle, and the scattering intensity units per unit volume, respectively. In Fig. 5a, the scattering intensity of each profile decreases monotonously with scattering vector $q(=2\pi s)$ and no clear scattering peaks are observed. In order to calculate the morphological parameters, such as the long period $L_{lamellae}$, the average lamellar thickness $d_{lamellae}$ and the invariant Q_{saxs}, the correlation function method was used. The details of this method have already been reported in a previous paper [21]. For the ideal two-phase system, the invariant is defined as

$$Q_{SAXS} = \phi_c(1-\phi_c)(\rho_c-\rho_a)^2 \tag{2}$$

where ϕ_c is the volume fraction of crystalline phase, which is given by

$$\phi_c \equiv \frac{d_{lamellae}}{L_{lamellae}} \tag{3}$$

and $(\rho_c - \rho_a)$ is the electron-density difference between the crystal and the amorphous phase. Of course, we have to take into account the electron-density of clay particles. However, owing to the small volume fraction of the clay in the range of 0.75–2.95%, it has a negligible effect on the electron-density difference. The obtained morphological parameters are summarized in Table 1. The value of ϕ_c is in good agreement with χ_c calculated from TMDSC analysis. Interestingly, both $d_{lamellae}$ and $L_{lamellae}$ are in same order of

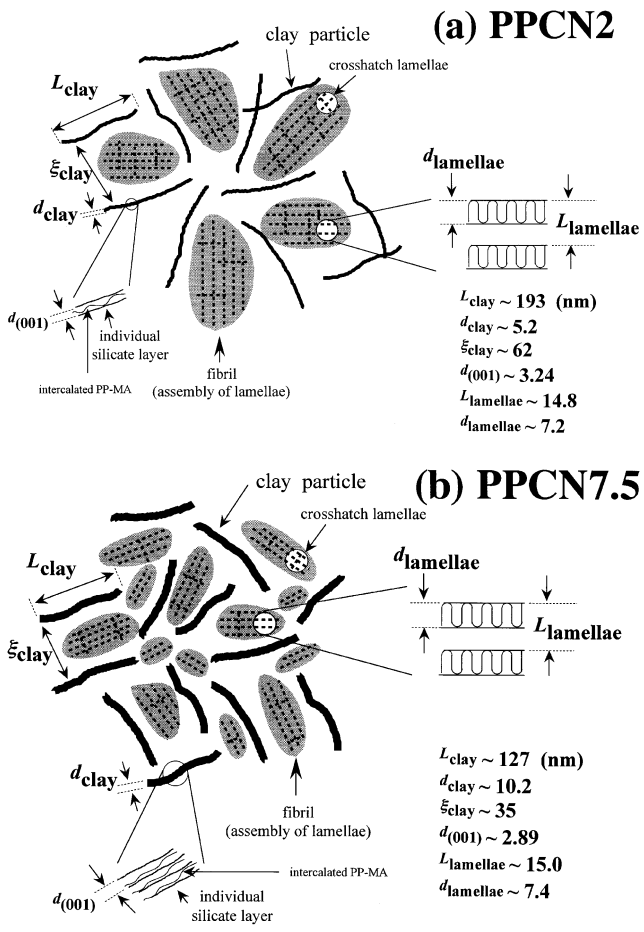

Fig. 6. The illustration for dispersed clay structure and the inter-fibrillar structure for: (a) PPCN2; and (b) PPCN7.5.

magnitude compared to d_{clay} and ξ_{clay}, respectively; and both of the lamellae parameters showed almost same values and are independent of the clay content. These values seem to be controlled by the crystallization temperature. After crystallization had taken place, the formation of the lamellae structure developed presumably in the space surrounded by the dispersed clay particles. This indicates that the dispersed clay particles are not located in the inter-lamellar region, i.e. the formation of the inter-fibrillar structure accompanied with fragmented lamellae surrounded by the dispersed clay particles can be speculated. The fragmented lamellae may be arranged parallel to each other by the surface of silicate layers. For example, in the space surrounded by the dispersed clay particles ($\cong \xi_{clay}$), the developed fibrils of the crystallized PPCN2 consist of about five lamellae and the clay particles are located in the space between two neighbor fibrils in the disordered spherulite. For the case of PPCN7.5, about three developed lamellae form one fibril. Thus, the presence of clay particle in the inter-fibrillar position makes the whole spherulite a disordered one. From the POM observation and obtained Hv–LS pattern, the illustration for dispersed clay structure and the inter-fibril structure is shown in Fig. 6. Thus, the intercalated PPCNs after

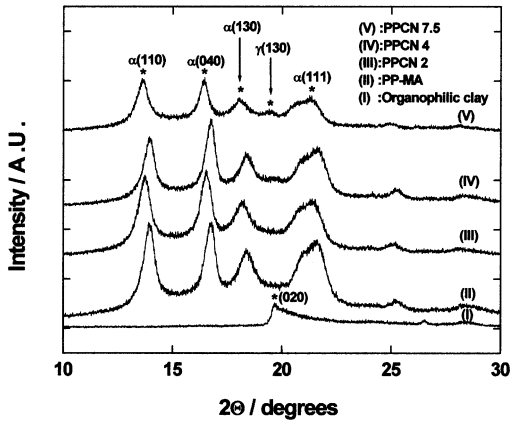

Fig. 7. WAXD patterns for organophilic clay, PP-MA, and PPCNs in the range of $2\theta = 10$–$30°$. The asterisks indicate the (110), (040), (130), and (111) planes for α-phase crystallite, the (130) plane for the γ-phase crystallite, and the (020) plane for silicate layers of organophilic clay. The diffraction curves are vertically offset for clarity.

crystallization have the hierarchical structure on the scale from nm to μm length.

3.3. γ-phase crystallite

Fig. 7 shows the WAXD patterns in the range of $2\Theta = 10$–$30°$ to explain the formation of γ-phase crystallite. The orthorhombic unit cell of the γ-phase crystallite consists of bilayers of two parallel helices with an inclination of 40° to the lamellar surface [22]. In Fig. 7, the diffraction peaks at $2\Theta = 13.9$, 16.7, 18.3, *and* 21.6° correspond to the planes (110), (040), (130), and (111) of α-phase crystallite, respectively [11,22]. The diffraction peak of (130) plane of γ-phase crystallite appears at $2\Theta = 19.3°$ as reported by Meille et al. [22]. Both the crystallized PPCN4 and PPCN7.5 exhibit a small peak around $2\Theta = 19.3°$ assigned to the reflection of (130) plane of γ-phase crystallite. The content of γ-phase X_γ is estimated according to Turner Jones method [23] from the ratio of the integral peak as given by

$$X_\gamma = \frac{I^\gamma_{(130)}}{I^\gamma_{(130)} + I^\alpha_{(130)}} \tag{4}$$

where $I^i_{(130)}$ is the integral peak of the (130) plane for each phase i. In this estimation, the diffraction peak at $2\Theta = 19.7°$ corresponding to the (020) plane of the individual silicate layers of the montmorillonite is observed near the (130) plane of γ-phase. However, an overlap effect of this diffraction peak is very weak due to the very small amount of clay as mentioned before. The calculated X_γ values increase with the addition of the clay as summarized in Table 1. The γ-phase in neat PP is only formed in some special cases such as isothermal crystallization under very high pressure [24] and crystallization of very low molecular weight fractions [25]. The enhancement of the formation of the γ-phase in neat PP takes place when the chainfolding in lamellae is forced to be more difficult as reported by

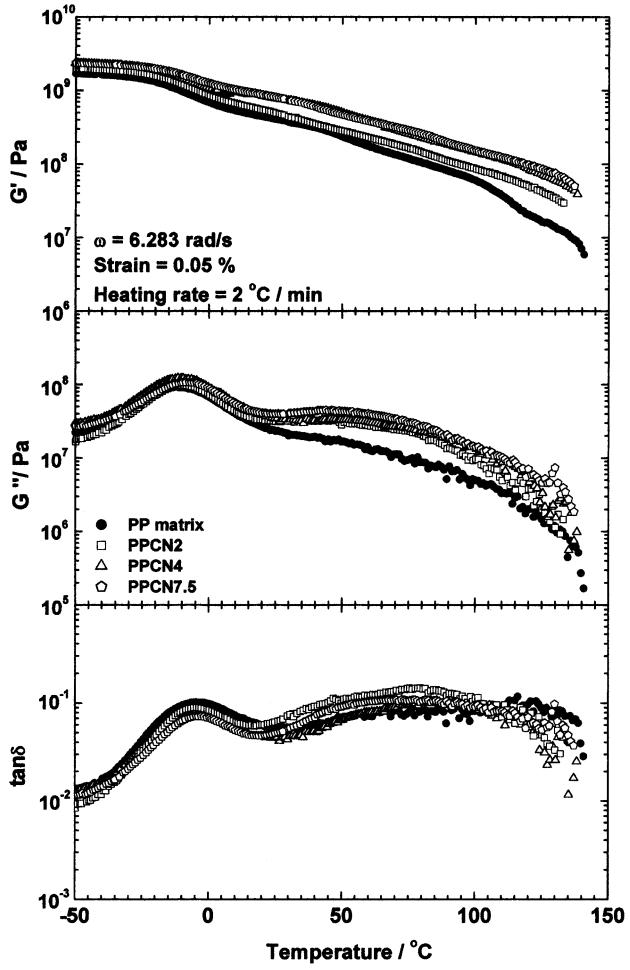

Fig. 8. Temperature dependence of storage G', loss G'' moduli and tan δ for the PP-MA and PPCNs.

Kressler et al. [26]. Presumably, the clay particles reduced the PP chain mobility owing to the narrow space surrounded by the dispersed clay particles ($\cong \xi_{clay} = 35$–50 nm) and the intercalation of the PP chains in silicate galleries. The reduction of the PP chain's mobility might lead to smaller, less-ordered crystallites. Furthermore, a measurable peak shift in crystalline chain–chain distance is observed not only for α-, but also for γ-phase with addition of the clay in WAXD patterns. The larger inter-chain distances may imply the formation of defect-ridden crystallites due to the reduction of chain diffusion into the lamellae.

Finally, one more interesting feature in the intercalated PPCNs is a possibility of the orientation and/or crystallization of the intercalated PP-MA chains in the silicate galleries because of the spatial confinement between very narrow space ($\cong d_{(001)}$). The confined orientation of the PP-MA chains will be discussed separately [18].

3.4. Mechanical properties and enhancement of modulus

Fig. 8 shows the plot for the temperature dependence of storage modulus G', loss modulus G'', and tan δ of the

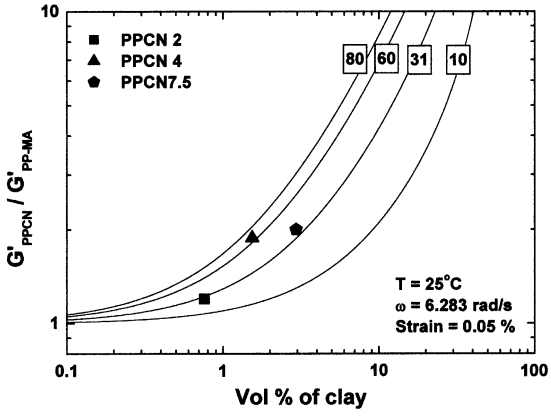

Fig. 9. Plots of $G'_{PPCN}/G''_{PP\text{-}MA}$ vs. volume% of clay for PPCNs. The value of Einstein coefficient, k_E, was shown in the box. The theoretical lines show the results calculated by Halpin–Tai's expression with various k_E.

intercalated PPCNs and PP-MA. The two peaks in tan δ curves are observed at −5°C and at high temperature around 50–90°C as a broad peak, respectively. The former corresponds to the T_g of the matrix polymer, and the latter to the T_m of the stearylammonium intercalated in the silicate gallery as shown in Fig. 1. The melting of the stearylammonium does not lead to a big drop in G' at this temperature range. The enhancement in moduli appears in different magnitudes at various temperature ranges. Below T_g, the enhancement of G' is clear in the intercalated PPCNs. At the temperature range of −50 to −10°C, the increments in G' are 16% for PPCN2, 40% for PPCN4 and 42% for PPCN7.5 as compared to that of PP-MA. Furthermore, at the temperature range of 0–110°C, both PPCN4 and PPCN7.5 exhibit higher enhancement in G' as compared to the PPCN2 and PP-MA. At 25°C, PPCN4 and PPCN7.5 show higher increment in G' of 90 and 100% than that of PP-MA, respectively, while that of PPCN2 is only 20% higher.

In Fig. 9, we summarized the clay content dependence of G' obtained at 25°C. For comparison, we show the ratio of $G'_{PPCN}/G'_{PP\text{-}MA}$. G'_{PPCN} and $G'_{PP\text{-}MA}$ are the moduli of the intercalated PPCNs and the PP-MA, respectively. The large reinforcement in G' is observed in the figure. As discussed previously [4], the essential factors governing the enhancement of mechanical properties is the aspect ratio of the dispersed clay particles. According to the Halpin and Tai's theoretical expression on the enhancement of G' [27], we estimate that the Einstein coefficient k_E is related to the aspect ratio of the dispersed clay particles. The details applicable to poly(methyl methacrylate) (PMMA)/clay nanocomposites was reported in a previous publication [4]. The k_E was estimated by selecting an appropriate value which best fit the experimentally obtained $G'_{PPCN}/G'_{PP\text{-}MA}$ vs. volume fraction of the clay plots. The estimated values of k_E were about 60 for PPCN4, and about 31 for PPCN2 and PPCN7.5. In the intercalated PPCNs, the explanation for the enhancement of G' by

only k_E factor as discussed in the previous case of PMMA/clay nanocomposites [4] is hampered because each PPCN exhibit different values of k_E, despite the different clay content. In the case of intercalated PPCNs, the enhancement of G' is probably due to both the degree of the intercalation and the aspect ratio of the dispersed clay particles. As shown in Table 1, the two-dimensional aspect ratio of the dispersed clay particles L_{clay}/d_{clay} estimated from TEM observation are 37 for PPCN2, 20 for PPCN4 and 12 for PPCN7.5, respectively. In the PPCN4, despite the lower value of L_{clay}/d_{clay} compared to PPCN2 and low addition of the clay compared to PPCN7.5, this nanocomposite shows the highest value of k_E, suggesting that much higher efficiency of the intercalation for the reinforcement is attained.

4. Conclusions

In this study, we demonstrated the hierarchical structure of the intercalated PPCNs viewed on scale from the structure of confined PP-MA chains in the space of the silicate galleries (intercalating sites) of 2–3 nm width to crystalline lamellae of 7–15 nm thickness and spherulitic texture of 10 μm diameter.

With increasing clay content, the PP-MA chains were intercalated in the space of the intercalating sites accompanied with the stacking of the individual silicate layers. In other words, the increment of intercalating sites leads to the limitation of the exfoliation toward the individual silicate layers. After crystallization had taken place, both $d_{lamellae}$ and $L_{lamellae}$ exhibited the same order of magnitude compared to d_{clay} and ξ_{clay}, respectively. Furthermore, both the lamella parameters showed almost same values and are independent of the clay content. The formation of the inter-fibrillar structure accompanied with fragmented lamellae between clay particles was speculated.

Owing to the narrow space surrounded by the dispersed clay particles and the intercalation of the PP chains in the space between silicate galleries, the formation of the γ-phase took place with the addition of clay.

The enhancement of moduli of the intercalated PPCNs was observed. To enhance the moduli, both the degree of intercalation of the PP-MA chains and the aspect ratio of the dispersed clay particles strongly affected the final mechanical properties of the PPCNs.

Acknowledgements

The present work was partially supported by the Grant-in-Aid for Academic Frontier Center under the project 'Future Data Storage Materials' granted by the Ministry of Education, Science, Sports and Culture (1999–2003).

References

[1] Usuki A, Kawasumi M, Kojima Y, Okada A, Kurauchi T, Kamigaito O. J Mater Res 1993;8:1174.
[2] LeBaron PC, Wang Z, Pinnavaia T. J Appl Clay Sci 1999;15:11.
[3] Alexandre M, Dubois P. Mater Sci Engng 2000;28:1.
[4] Okamoto M, Morita S, Kim YH, Kotaka T, Tateyama H. Polymer 2001;42:1201.
[5] Okamoto M, Morita S, Kotaka T. Polymer 2001;42:2685.
[6] Vaia RA, Ishii H, Giannelis EP. Chem Mater 1993;5:1694.
[7] Hasegawa N, Okamoto H, Kato M, Usuki A. J Appl Polym Sci 2000;78:1981.
[8] Hasegawa N, Okamoto H, Kato M, Tsukigase A, Usuki A. Macromol Mater Engng 2000;280/281:76.
[9] Huang JC, Zhu Z-K, Yin J, Qian X-F, Sun YY. Polymer 2001;42:873.
[10] Cho JW, Pail DR. Polymer 2001;42:1083.
[11] Moore Jr EP. Polypropylene Handbook. Cincinnati: Hanser/Gardner, 1996.
[12] Galgali G, Ramesh C, Lele A. Macromolecules 2001;34:852.
[13] Solomon MJ, Almusallam AS, Seefeld KF, Somwangthanaroj S, Varadan P. Macromolecules 2001;34 appeared in ACS website.
[14] Wunderlich B, Jin Y, Boller A. Thermochim Acta 1994;238:277.
[15] Okamoto M, Kubo H, Kotaka T. Macromolecules 1999;32:6206.
[16] Okamoto M, Kubo H, Kotaka T. Macromolecules 1998;31:4223.
[17] Norton BR, Keller A. Polymer 1985;26:704.
[18] Maiti P, Nam PH, Okamoto M, Kotaka T, Macromol (submitted).
[19] Stroble GR. Acta Crystallogr (A) 1970;26:367.
[20] Stroble GR. The Physics of Polymers. Berlin: Springer, 1997.
[21] Okamoto M, Inoue T. Polymer 1995;36:2739.
[22] Meille S, Bruckner S, Porzio W. Macromolecules 1990;23:4114.
[23] Turner Jones A, Aizlewood JM, Beckett DR. Macromol Chem 1964;75:134.
[24] Kardos JL, Christiansen E, Baer E. J Polym Sci 1966;A2(4):777.
[25] Kojima M. J Polym Sci 1968;A2(6):1255.
[26] Thomann R, Semke H, Maier RD, Thomann Y, Scherble J, Mulhäupt R, Kressler J. Polymer 2001;42:4597.
[27] Nielsen LE. Mechanical Properties of Polymers and Composites. New York: Marcel Dekker, 1975.